Coherent control of photocurrents in graphene and carbon nanotubes

E. J. Mele
Department of Physics and Laboratory for Research on the Structure of Matter, University of Pennsylvania, Philadelphia, Pennsylvania 19104

Petr Král
Department of Physics, University of Toronto, Toronto, Ontario M5S 1A7, Canada

David Tománek
Department of Physics and Astronomy, Michigan State University, East Lansing, Michigan 48824
(Received 3 September 1999)

Coherent one-photon (2ω) and two-photon (ω) electronic excitations are studied for graphene sheets and for carbon nanotubes using a long-wavelength theory for the low-energy electronic states. For graphene sheets we find that a coherent superposition of these excitations produces a polar asymmetry in the momentum space distribution of the excited carriers with an angular dependence that depends on the relative polarization and phases of the incident fields. For semiconducting nanotubes we find a similar effect which depends on the square of the semiconducting gap, and we calculate its frequency dependence. We find that the third-order nonlinearity, which controls the direction of the photocurrent is robust for semiconducting tubes and vanishes in the continuum theory for conducting tubes. We calculate corrections to these results arising from higher-order crystal-field effects on the band structure and briefly discuss some applications of the theory.

I. INTRODUCTION

The magnitude and direction of photocurrents in semiconductors are ordinarily controlled using applied bias voltages. Interestingly the direction of a photocurrent in a semiconductor can also be controlled without bias voltages through phase coherent control of the incident optical fields. In a typical experiment an initial and final state are simultaneously coupled using two coherent excitations: one photon excitation at frequency 2ω and two photon excitation at frequency ω. The coherent superposition of these two excitations can lead to a polar asymmetry in the momentum space distribution of the excited photocarriers and therefore to a net photocurrent. The effect has been discussed theoretically[1,2] and observed experimentally in photoyield from atoms[3] and for photocurrents in semiconductors.[4] Recently, two of us have proposed that for carbon nanotubes this effect could provide directional control of a photocurrent along the tube axis[5] and even suggests a novel method for biasing the diffusion of ionic species which intercalate within the nanotubes.

In this paper, we study the excitations that lead to this effect both for graphene sheets and for carbon nanotubes. In both these systems the low-energy electronic properties relevant to most solid state effects are determined by an interesting feature of the band structure. The isolated graphene sheet has only an incipient Fermi surface; it is actually a zero gap semiconductor where the conduction and valence bands meet at precise points in momentum space. The carbon nanotube is a cylindrical tubule formed by wrapping a graphene sheet and for metallic tubes the ''zero gap'' feature manifests itself in a peculiar doubling of the low energy electronic spectrum with ''pairs'' of forward and backward moving excitations at both k_F and $-k_F$.[6] In either case, the low-energy electronic spectra are described by a two-component Dirac Hamiltonian.[6]

In this paper, we develop the theory of phase coherent one- and two-photon excitation within this model. The application to the graphene sheet turns out to be a useful pedagogical model, which is unusual for a semiconductor and nicely illustrates the origin of phase coherent control of photocurrents for a graphene derived system. For graphene it is inappropriate to analyze the third-order nonlinearity by analogy with the third-order response in atomic systems, as has been done previously for semiconductors.[4] Instead, we find that the third-order response probes the rather unique geometry of the extended low-energy electronic eigenstates which occur within the graphene sheet. The application of the model to a carbon nanotube shows, interestingly, that the third-order nonlinearity is suppressed for excitations between the lowest subbands of any conducting nanotube and vanishes completely for transitions between the lowest subbands of a conducting ''armchair'' tube, but it is nonzero and robust for the gapped subbands of a semiconducting tube. In fact, the effects we calculate are significantly stronger for semiconducting nanotubes than for a conventional semiconductor. In principle this effect might be used to distinguish conducting and semiconducting tubes in a compositionally mixed sample. Other possible applications of the idea will be discussed later in the paper.

In this paper, we briefly review the effective mass theory for the graphene sheet in Sec. II. In Secs. III and IV, we derive the interaction terms in the long-wavelength theory, which couple the electrons to time varying electromagnetic fields and present a calculation of the coherent third-order nonlinear optical excitations using this model. Section V applies the results to study the third-order response of an isolated infinite graphene sheet. In Sec. VI, we use the theory to

 ©2000 The American Physical Society

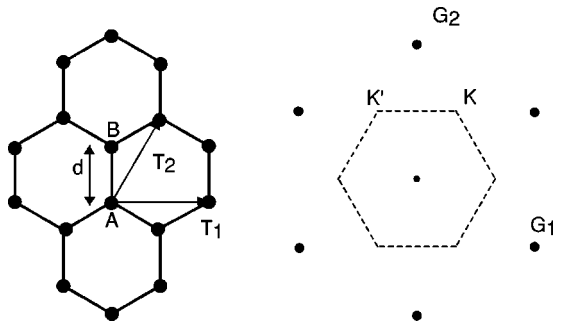

FIG. 1. Direct and reciprocal space structures of the graphene lattice. The primitive cell contains two sublattice sites labeled *A* and *B* in the left panel. The right panel shows the first star of reciprocal-lattice vectors and the first Brillouin zone. The long-wavelength theory expands the electronic Hamiltonian for momenta near the *K* and K' points at the Brillouin-zone corners.

study third-order effects for conducting and semiconducting carbon nanotubes. A discussion and some applications of the results are presented in Sec. VII.

II. EFFECTIVE MASS THEORY

In this section, we briefly review the effective mass description of the low-energy electronic states. The theory is developed for an ideal graphene sheet, a section of which is shown in Fig. 1. The primitive cell of this structure contains two atoms, labeled *A* and *B* in the figure. The lattice is unchanged after a translation by any combination of the two primitive translations vectors

$$\vec{T}_1 = a(1,0),$$

$$\vec{T}_2 = a\left(\frac{1}{2}, \frac{\sqrt{3}}{2}\right), \tag{1}$$

where the bond length $d = a/\sqrt{3}$. We introduce a pair of primitive translation vectors for the reciprocal lattice $\vec{G}_i$ such that $\vec{G}_i \cdot \vec{T}_j = 2\pi\delta_{ij}$, yielding

$$\vec{G}_1 = \frac{4\pi}{\sqrt{3}a}\left(\frac{\sqrt{3}}{2}, -\frac{1}{2}\right)$$

$$\vec{G}_2 = \frac{4\pi}{\sqrt{3}a}(0,1) \tag{2}$$

which generate a triangular lattice in reciprocal space.

The critical points $K(K')$ are important to our discussion, and they occur at the corners of the Brillouin zone of this reciprocal lattice at the positions

$$K = \frac{1}{3}(\vec{G}_1 + 2\vec{G}_2) = \frac{4\pi}{3a}\left(\frac{1}{2}, \frac{\sqrt{3}}{2}\right),$$

$$K' = \frac{1}{3}(-\vec{G}_1 + \vec{G}_2) = \frac{4\pi}{3a}\left(-\frac{1}{2}, \frac{\sqrt{3}}{2}\right). \tag{3}$$

The ''bonding'' and ''antibonding'' π electron bands meet precisely at these $K(K')$ points in reciprocal space. This band touching is required by symmetry for this system and it is correctly described by the simplest model for electron propagation within the graphene sheet which is a tight-binding model in which the hopping of an electron between neighboring sites is set by a single energy, *t*. Thus, we have

$$h_{\mu\nu} = \langle \phi_\mu | H | \phi_\nu \rangle = t \quad (\text{nearest-neighbor} \quad \mu\nu)$$

$$= 0 \quad (\text{otherwise}). \tag{4}$$

Working in the sublattice basis and at crystal momentum $\vec{k}$ we have the Hamiltonian

$$H(\vec{k}) = t\begin{pmatrix} 0 & 1 + e^{-i\vec{k}\cdot\vec{T}_2} + e^{-i\vec{k}\cdot(\vec{T}_2 - \vec{T}_1)} \\ 1 + e^{i\vec{k}\cdot\vec{T}_2} + e^{i\vec{k}\cdot(\vec{T}_2 - \vec{T}_1)} & 0 \end{pmatrix}. \tag{5}$$

If we set $\vec{k} = \vec{K} + \vec{q}$ and expand the Hamiltonian for $qa \ll 1$ we obtain the long-wavelength Hamiltonian

$$H_K(\vec{q}) = \frac{\sqrt{3}ta}{2}\begin{pmatrix} 0 & q_x + iq_y \\ q_x - iq_y & 0 \end{pmatrix} = \hbar v_F \vec{\sigma}^* \cdot \vec{q}, \tag{6}$$

where $\vec{\sigma}$ are the 2×2 Pauli matrices. A similar expansion near the K' point yields

$$H_{K'} = -\hbar v_F \vec{\sigma} \cdot \vec{q}. \tag{7}$$

Identifying each of the critical points with the index α so that $\alpha = 1$ denotes the *K* point and $\alpha = -1$ denotes the K' point, these Hamiltonians can be rotated into diagonal form with the unitary operators

$$U_\alpha(\vec{q}) = \frac{1}{\sqrt{2}}\begin{pmatrix} 1 & 1 \\ -\alpha e^{-i\alpha\theta} & \alpha e^{-i\alpha\theta} \end{pmatrix}, \tag{8}$$

where $\theta = \tan^{-1}(q_y/q_x)$. Thus,

$$U_\alpha^\dagger(\vec{q}) H_\alpha(\vec{q}) U_\alpha(\vec{q}) = \hbar v_F \begin{pmatrix} -|q| & 0 \\ 0 & |q| \end{pmatrix}, \tag{9}$$

so that Eqs. (6) and (7) describe pairs of bands that disperse linearly away from the critical *K* and K' points. Note also that $H_\alpha(\vec{q}) = H^*_{-\alpha}(-q)$ as expected. Equations (6) and (7) and the unitary rotations in Eq. (8) provide the appropriate description of all the low energy electronic excitations required for this problem.

III. GRAPHENE-FIELD INTERACTION HAMILTONIAN

In this section we collect several results we need to describe the coupling of electrons described by Eqs. (6) and (7) to the electromagnetic potentials. For a particle of charge *Q* interacting with the electromagnetic vector potential $\vec{A}$ and scalar potential Φ the momentum and energy are shifted $\vec{p} \rightarrow \vec{p} - Q\vec{A}/c$ and $E \rightarrow E - Q\Phi$.[7] Thus, the interaction Hamiltonian that couples the Dirac particle to the time varying vector potential (A_x, A_y) is

$$H_{\alpha,int} = -\alpha v_F Q(A_x\sigma_x - \alpha A_y\sigma_y)/c. \tag{10}$$

This interaction operator can also be obtained by calculating the velocity operator from the commutator of the position operator with the unperturbed Hamiltonian:

$$\vec{v}_\alpha = \frac{i}{\hbar}[H_\alpha, \vec{r}] \tag{11}$$

and therefore

$$\vec{v}_\alpha = \alpha v_F(\sigma_x, -\alpha\sigma_y) \tag{12}$$

so that $H_{\alpha,int} = -\vec{j}_\alpha \cdot \vec{A}/c$.

It is useful to rotate the interaction Hamiltonian (10) into the band basis using the unitary operators in Eq. (8). To do this we write $\hat{q} = (q_x, q_y)/|\vec{q}|$ and compute $H^b_{\alpha,int} = U^\dagger_\alpha(\hat{q}) H_{\alpha,int}(\hat{q}) U_\alpha(\hat{q})$ giving

$$H^b_{\alpha,int}(\hat{q},\vec{A}) = \frac{ev_F}{c}\begin{pmatrix} -\hat{q}\cdot\vec{A} & -i\alpha\hat{z}\cdot(\hat{q}\times\vec{A}) \\ i\alpha\hat{z}\cdot(\hat{q}\times\vec{A}) & \hat{q}\cdot\vec{A} \end{pmatrix}. \tag{13}$$

This demonstrates that the coupling between the Bloch electrons and the vector potential depends on the angle between $\vec{v}$ and $\vec{A}$ and that the interband matrix elements [which are the off-diagonal terms in Eq. (13)] vanish when the two are collinear. Indeed, $H_\alpha(\vec{q})$ and $H_{\alpha,int}(\hat{q},\vec{A})$ commute along these special lines in reciprocal space, so that interband transitions are forbidden along this trajectory. This peculiar feature can be traced to the absence of a mass term in the effective Hamiltonians in Eqs. (6) and (7) which would ordinarily mix the plane-wave solutions to Eqs. (6) and (7) and thereby allow interband transitions by coupling with the long-wavelength current operator. When $\vec{v}$ and $\vec{A}$ are not collinear interband transitions are allowed and the transition amplitudes are fixed by the mismatch in their orientations in the graphene plane. This has interesting consequences for coherent control of nonlinear optical processes in the nanotubes, as we show below.

IV. NONLINEAR OPTICAL EXCITATIONS

In this section, we present a calculation of the transition probabilities for the third-order nonlinear optical excitations among the electronic states given by the models in Secs. II and III. We introduce time varying fields of the form

$$\vec{A}(\vec{r},t) = \vec{A}_\omega e^{-i\omega t + i\phi_1} + \vec{A}_{2\omega} e^{-2i\omega t + i\phi_2} + \text{c.c.} \tag{14}$$

and study the response of the system to third order in these exciting fields. Asymmetries in the photocurrent are controlled by the coherent excitation of electrons from an initial state to a final state by one photon (2ω) and by two one photon (ω) processes. The coherent mixing of these two processes is studied by evolving the density matrix to third order in the exciting fields and isolating the terms proportional to $A_\omega A_\omega A_{-2\omega}$.

It is convenient to study the time evolution of the one particle density matrix $\rho = \langle \Psi^\dagger(\vec{r})\Psi(\vec{r}')\rangle$. The Hamiltonian for our system is $H_\alpha + H_{\alpha,int}$ and we work in the Heisenberg representation so that

$$\frac{d\rho}{dt} = \frac{i}{\hbar}[H_{\alpha,int}(t), \rho], \tag{15}$$

where H_α is the free particle Hamiltonian and $H_{\alpha,int}(t) = e^{iH_\alpha t} H_{\alpha,int} e^{-iH_\alpha t}$. In the band basis the density matrix in the initial state has the form

$$\rho_0 = \rho(t=-\infty) = \begin{pmatrix} 1 & 0 \\ 0 & 0 \end{pmatrix} \tag{16}$$

since only the negative energy states of the Hamiltonians (6) and (7) are initially occupied.

We expand the density matrix order by order in the exciting fields

$$\rho(t) = \rho_0 + \rho_1 + \rho_2 + \rho_3 + \cdots. \tag{17}$$

Integrating Eq. (17) to first order in the applied fields gives

$$\rho_1 = \frac{iev_F}{\hbar c}\begin{pmatrix} 0 & F_1(t) \\ -F_1^*(t) & 0 \end{pmatrix}, \tag{18}$$

where

$$\begin{aligned} F_1(t) = {} & \frac{\alpha\hat{z}\cdot(\hat{q}\times\vec{A}_\omega)e^{-i(\Delta+\omega)t+i\phi_1}}{-\Delta-\omega-i\delta} \\ & + \frac{\alpha\hat{z}\cdot(\hat{q}\times\vec{A}_{-\omega})e^{-i(\Delta-\omega)t-i\phi_1}}{-\Delta+\omega-i\delta} \\ & + \frac{\alpha\hat{z}\cdot(\hat{q}\times\vec{A}_{2\omega})e^{-i(\Delta+2\omega)t+i\phi_2}}{-\Delta-2\omega-i\delta} \\ & + \frac{\alpha\hat{z}\cdot(\hat{q}\times\vec{A}_{-2\omega})e^{-i(\Delta-2\omega)t-i\phi_2}}{-\Delta+2\omega-i\delta}, \end{aligned} \tag{19}$$

where $\Delta = 2v_F q$ and δ is a positive infinitesimal.

The second-order terms ρ_2 include the lowest-order changes to the occupation probabilities which can be induced with excitation by the ω or the 2ω fields

$$\begin{aligned} (\dot{\rho}_2)_{22} = -(\dot{\rho}_2)_{11} = {} & \frac{2\pi e^2 v_F^2}{\hbar^2 c^2}[|\alpha\hat{z}\cdot(\hat{q}\times\vec{A}_\omega)|^2\delta(\Delta-\omega) \\ & + |\alpha\hat{z}\cdot(\hat{q}\times\vec{A}_{2\omega})|^2\delta(\Delta-2\omega)] \end{aligned} \tag{20}$$

as well as oscillating nonlinear off-diagonal coherence terms

$$(\rho_2)_{12} = -\frac{ie^2 v_F^2}{\hbar^2 c^2} F_2(t). \tag{21}$$

Anticipating the situation $2\omega \approx \Delta$, the most important contribution to $F_2(t)$ has the form

$$F_2(t) = \frac{(\hat{q}\cdot\vec{A}_{-\omega})(\alpha\hat{z}\cdot\hat{q}\times\vec{A}_{-\omega})e^{-i(\Delta-2\omega)t-2i\phi_1}}{(-\Delta+\omega-i\delta)(-\Delta+2\omega-i\delta)}. \tag{22}$$

The second-order coherence term in Eq. (22) leads to a transition rate, which is third order in the applied fields and is the source of the polar asymmetry of the photocurrent,

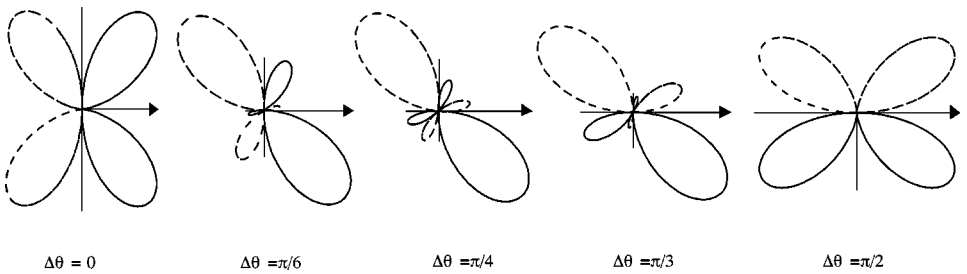

FIG. 2. Angular distributions of the transition rates given by Eq. (23). In each panel the $\vec{A}_\omega$ is polarized along the horizontal direction (the direction of the arrow in each plot) and $\Delta\theta$ is the angle between the $\vec{A}_{2\omega}$ and $\vec{A}_\omega$ fields. The polar plot gives the transition rate as a function of the angle of the Bloch wave vector $\hat{q}$ with respect to the direction of $\vec{A}_\omega$. These angular distributions are superimposed on the angular distribution for the direct transition rate, which is given by the second term in Eq. (20). The solid curves correspond to $(\dot{\rho}_3)_{22}>0$, dashed curves to $(\dot{\rho}_3)_{22}<0$ when $\cos(\phi_2-2\phi_1)>0$.

$$(\dot{\rho}_3)_{22}=\frac{8\pi e^3 v_F^3}{\Delta\hbar^3 c^3}\mathrm{Re}[(\alpha\hat{z}\cdot\hat{q}\times\vec{A}_{2\omega})(\hat{q}\cdot\vec{A}_{-\omega}) \times(\alpha\hat{z}\cdot\hat{q}\times\vec{A}_{-\omega})e^{i(\phi_2-2\phi_1)}]\delta(\Delta-2\omega). \quad (23)$$

Equation (23) contains a factor of two from the sum over the (physical) spins. Equation (23) presents the main result of the paper. It shows that the transition rate depends on the polarization and phases of both exciting fields and the Bloch wave vector $\vec{q}$. We will explore the consequences of the geometric structure of this result for the graphene sheet and for carbon nanotubes in the following two sections. For the moment, we note that the result is odd in the direction of the Bloch wave vector $\hat{q}$ and even in the critical point index α (it depends on α^2) and therefore the symmetry breaking nonlinearity is nonzero after integration over the full Brillouin zone.

V. APPLICATION TO GRAPHENE

In this section, we apply the formalism developed in Sec. III to study the coherent optical control of photocurrents for a single-graphene sheet. The model nicely illustrates the selection rules which apply in this geometry, and the results can be extended to analyze the more complex situation for the nanotube, which will be presented in Sec. VI.

We note that both Eqs. (20) and (23) contain terms that describe transitions from the valence to the conduction band at the frequency $2\omega=\Delta$. Equation (20) is the ordinary linear absorption in the material. Interestingly, we see that the angular distribution of the excited photocarriers is not isotropic but rather follows a $\sin^2\phi$ dependence with respect to the polarization of the exciting radiation. Nevertheless, this angular distribution has even parity and thus does not produce a net current. On the other hand, Eq. (23) gives an angular distribution that breaks the inversion symmetry of the graphene sheet. The symmetry breaking is actually implicit in the coherent superposition of the exciting fields. We will estimate the prefactors to compare the relative strengths of these terms for accessible laboratory fields later in the paper; for the moment we note that the nonlinear terms in Eq. (23) typically contribute $\approx 10^{-3}$ of the total transition rate, and thus the induced anisotropy while nonzero (and we believe measurable) is a subtle effect.

The angular distribution in Eq. (23) is controlled by the relative polarizations and phases of the incident $\vec{A}_\omega$ and $\vec{A}_{2\omega}$ fields. Figure 2 displays polar plots of the angular distributions for the situation where the amplitudes are in phase [i.e., $\vec{A}_\omega$ and $\vec{A}_{2\omega}$ in Eq. (14) are presumed to be real] for various incident polarizations. Note that the underlying electronic dispersion relations are completely isotropic in the linearized theory, and thus only the relative polarization of the two exciting fields is relevant for the interference pattern. In all cases $\vec{A}_\omega$ is taken to be polarized along the horizontal direction shown by the arrow in the plots. In each plot, we observe a node in the current distribution along this direction. This follows from the symmetry of $H^b_{\alpha,int}$ in Eq. (13), which shows that interband coupling is prohibited for $\hat{q}$ parallel to $\vec{A}$. Nonetheless, the situation for collinear ω and 2ω excitation clearly shows the asymmetry between the ''forward'' and ''backward'' distribution of the photocurrent. The situation is more interesting when the exciting fields are noncollinear. We observe that the angular distribution develops a ''three lobe'' structure. Ultimately, when the exciting fields area mutually orthogonal, we recover the ''two lobe'' pattern with the angular distribution rotated by $\pi/2$ with respect to the polarization of the incident ω field. It is useful to quantify the anisotropy of the distribution by calculating the average polarization of the net photocurrent $\langle\cos\phi\rangle$ and $\langle\sin\phi\rangle$ averaged over this distribution. One finds

$$\langle\cos\phi\rangle=\frac{1}{2}\cos\theta$$

$$\langle\sin\phi\rangle=-\frac{1}{2}\sin\theta \quad (24)$$

so that when the 2ω field is tipped by an angle θ with respect to the ω field, the photocurrent is oriented in the direction $-\theta$. Finally, the ''sign'' of the effect is determined by the relative phases of the two exciting fields. Note that the phase delays ϕ_1 and ϕ_2 in the exciting fields of Eq. (14) modulate the transitions rates[4] in Eq. (23) in the combination

$$(\dot{\rho}'_3)_{22}\rightarrow(\dot{\rho}_3)_{22}\cos(\phi_2-2\phi_1). \quad (25)$$

This does not change the qualitative features of the angular distribution but it can modify both its magnitude and its overall sign.

Thus the angular distribution in the collinear case $\Delta\theta=0$ can be reversed by advancing the phase of the ω fields by $\pi/2$.

VI. APPLICATION TO NANOTUBES

A. Low-Energy Theory for Semiconducting Tubes

In this section, we apply the formalism of Sec. III to study phase coherent control of a photocurrent on a carbon nanotube. The essential complication is that the wrapped structure of the nanotube quantizes the allowed crystal momenta so that the transition rate automatically contain an intrinsic anisotropy. Nevertheless, the formalism developed in Sec. III can be extended to include this situation.

We first define the geometry for the single-wall nanotube. The nanotube is a cylinder formed by wrapping a graphene sheet and the wrapping can be defined by the graphene superlattice translation vector around the tube waist. We adopt the primitive vectors of Eq. (1) as a basis and represent the superlattice translation $\vec{T}_{MN}$ as

$$\vec{T}_{MN}=M\vec{T}_1+N\vec{T}_2=\left(M+\frac{N}{2},\frac{\sqrt{3}N}{2}\right)a. \tag{26}$$

It is useful to define two unit vectors defining the longitudinal and azimuthal directions within the graphene plane

$$\hat{e}_l=(\cos\theta_c,\sin\theta_c)$$

$$\hat{e}_a=(-\sin\theta_c,\cos\theta_c), \tag{27}$$

where $\theta_c=\cos^{-1}(M+N/2)/(\sqrt{M^2+N^2+MN})$ is the chiral angle of the tube. The wrapping of the tube quantizes the allowed momenta along the azimuthal direction $\vec{k}\cdot\hat{e}_a=2\pi n/(a\sqrt{M^2+N^2+MN})$ while the electrons obey free particle boundary conditions along the tube direction and the longitudinal component $\vec{k}\cdot\hat{e}_l$ can take any value.[8–10] Thus, the loci of allowed momenta are ''lines'' in reciprocal space. These lines need not intersect the critical K and K' points, which are used as a reference for the long-wavelength theory. To determine the mismatch between the allowed crystal momenta and the K and K' point wave functions we resolve the Bloch wave vector at K and K' into its longitudinal and azimuthal components. We find

$$K_\alpha=\frac{4\pi}{3a}\left(\frac{\alpha}{2},\frac{\sqrt{3}}{2}\right) \tag{28}$$

and

$$K_\alpha\cdot\hat{e}_a=\frac{2\pi}{3a}\left[\frac{2\alpha M+N(3+\alpha)}{2\sqrt{M^2+N^2+MN}}\right], \tag{29}$$

which lies along the locus of allowed wave vectors when $2\alpha M+(3+\alpha)N=6n$. One third of the (M,N) tubes satisfy this condition, and for the remaining two thirds of the tubes the $K(K')$ momenta are mismatched to the kinematically allowed momenta by a minimum amount

$$\Delta_\alpha=\frac{2\pi}{3a\sqrt{M^2+N^2+MN}}(-1)^{\mathrm{mod}(\alpha(N-M),3)}. \tag{30}$$

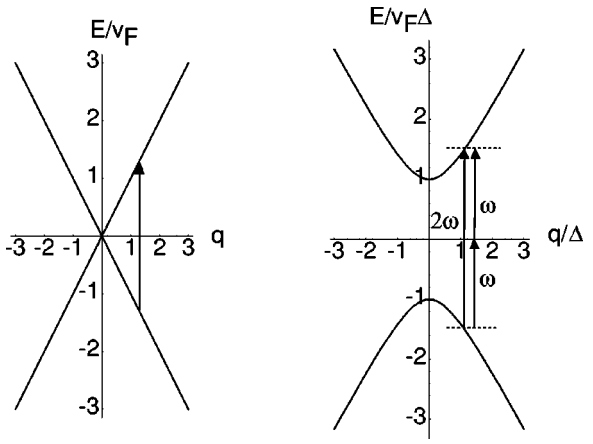

FIG. 3. Optical excitation between lowest subbands of a conducting tube (left panel) are forbidden in the long-wavelength theory. They are allowed for a semiconducting tube (or for the gapped subbands of a conducting tube) as shown on the right. Δ denotes the crystal momentum mismatch between the valence and conduction band states and the $K(K')$ points of the graphene sheet. The right-hand panel illustrates one- and two-photon excitations, which interfere to produce a polar asymmetry in the photocurrent.

Representing the ''reduced'' Bloch wave vector with the complex number $\tilde{q}=q_x+iq_y=qe^{i\theta_c}$ and the momentum mismatch by $\tilde{\Delta}_\alpha=i\Delta e^{i\theta_c}$ after a rotation of the coordinate system by the chiral angle θ_c (so that the x axis runs parallel to the tube length) the Hamiltonians in Eqs. (6) and (7) can be written

$$H_\alpha(q)=\hbar v_F\begin{pmatrix}0 & \alpha q+i\Delta_\alpha\\ \alpha q-i\Delta_\alpha & 0\end{pmatrix}. \tag{31}$$

Note that in Eq. (31) $H_\alpha(q)=H^*_{-\alpha}(-q)$. The spectrum is now $E(q)=\pm\sqrt{q^2+\Delta^2}$ and the Hamiltonian is diagonalized with the unitary transformation

$$U_\alpha(q)=\frac{1}{\sqrt{2}}\begin{pmatrix}1 & 1\\ -\alpha e^{-i\alpha\gamma} & \alpha e^{-i\alpha\gamma}\end{pmatrix}, \tag{32}$$

where $\gamma=\tan^{-1}(\Delta/q)$. This is the rotation identified in Eq. (8) for the unfolded graphene sheet with Δ playing the role of the y component of the momentum. With this identification the interaction Hamiltonian for the nanotube analogous to Eq. (13) in the band basis is

$$H^b_{\alpha,int}(q,A)=\frac{ev_FA}{c}\frac{1}{\sqrt{q^2+\Delta^2}}\begin{pmatrix}-q & i\alpha\Delta\\ -i\alpha\Delta & q\end{pmatrix}. \tag{33}$$

Note that the off-diagonal terms which describe the amplitudes for interband transitions depend explicitly on the size of the semiconducting backscattering gap Δ and vanish for the lowest subbands of a conducting nanotube as shown in Fig. 3.

Thus, when the exciting fields are collinear and directed along the tube direction the third-order transition rate is

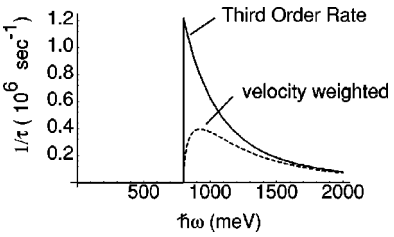

FIG. 4. Frequency dependence of the third-order transition rate leading to anisotropy of the photocurrent. The solid curve gives the transition rate of Eq. (30) as a function of the exciting frequency $\hbar\omega$. To display the spectra we have taken a semiconducting gap $\hbar v_F\Delta=800$ meV and normalized the incident intensity so that $|A|=10^{-9}$ T-m at all frequencies. The dashed curve is the transition rate weighted by the final state velocity. Band-edge states are strongly scattered by the mass term and do not contribute effectively to the photocurrent.

$$(\dot{\rho}_3)_{22}=\frac{4\pi\alpha^2e^3v_F^6}{\hbar^2c^3\omega^4}\Delta^2 q\,\mathrm{Re}\,(A_{2\omega}A_{-\omega}A_{-\omega}e^{i(\phi_2-2\phi_1)})\times\delta[2E(q)-2\hbar\omega]. \tag{34}$$

Equation (34) is the origin of the asymmetry discussed in Ref. 5. We note that the result depends on the square of the magnitude of the gap Δ and it vanishes for transitions between the lowest subbands of a conducting tube. The result is odd in the reduced momentum q which produces an asymmetry between forward and backward moving photocarriers. The third-order transition rate is very small for high exciting frequency since the high-energy electrons are very weakly backscattered through the mass term in Eq. (31) and behave essentially as free particles. These properties are displayed in Fig. 4 which shows the third-order transition rate between two bands of a semiconducting tube as a function of the exciting frequency. It is interesting to note that the expected divergence in the one dimensional density of states at threshold is exactly canceled by the momentum prefactor q in Eq. (34) and thus the spectrum shows only a steplike singularity at the threshold. Thus, the transition probability for right- and left-moving photocarriers jumps discontinuously across the critical point at $q=0$. Note however that the states near the band gap have no group velocity and cannot contribute to the photocurrent so the velocity weighted transition rate (which is more relevant to this application) goes to zero at threshold. This is shown by the dashed curve in Fig. 4. The results in Fig. 4 show the nonlinear injection rate for a perfect defect free semiconducting tube. A slowly varying impurity potential (long range disorder in the notation of Ref. 12) can produce an additional channel for backscattering and will therefore further suppress the group velocity for electronic states near the band edges. In the presence of disorder, we therefore expect an additional rounding of the current injection rate, similar to that shown as the dashed curve in Fig. 4. The range and strength of this suppression will depend sensitively on the details of the long-range impurity potential. The results of Fig. 4 are insensitive to this additional backscattering deeper into the particle-hole continuum.

B. Crystal-field effects for conducting tubes

Equation (34) gives the third-order nonlinear response in the long-wavelength limit where we can linearize the electronic bands around the critical $K(K')$ points. Corrections to this result can be obtained in an expansion in qa and physically arise from crystal-field (''trigonal warping'') effects in the underlying band structure. The most significant such corrections occur for conducting tubes. Equation (34) gives a vanishing transition rate for excitations between the lowest bands of a conducting tube and trigonal warping of the band structure of the graphene sheet provides a mechanism to ''turn on'' these transitions even for conducting tubes. Thus a third-order nonlinear response is symmetry allowed for the lowest subbands of a conducting nanotube, though it strictly vanishes in the long-wavelength limit we have discussed so far.

To investigate the trigonal warping effects we rederive the interaction Hamiltonian without adopting the effective mass representation. To do this we note that in the presence of a vector potential $\vec{A}$ the Hamiltonian (5) is perturbed through the Peierls substitution $\vec{k}\rightarrow\vec{k}-(Q/c)\vec{A}$. Therefore, we can calculate the current operator using $j_\mu=-\partial H/\partial A_\mu=(Q/c)\partial H/\partial k_\mu$. In the site representation the Hamiltonian has only off-diagonal elements, so we can write

$$H_{int}=-\frac{e}{c}\vec{A}\cdot\begin{pmatrix}0 & \nabla_k t(\vec{k})\\ \nabla_k t^*(\vec{k}) & 0\end{pmatrix}. \tag{35}$$

We also note that the Hamiltonian is diagonalized with the unitary transformation:

$$U(\vec{k})=\frac{1}{\sqrt{2}}\begin{pmatrix}1 & 1\\ -\dfrac{t^*(\vec{k})}{|t(\vec{k})|} & \dfrac{t^*(\vec{k})}{|t(\vec{k})|}\end{pmatrix}, \tag{36}$$

which is the discrete lattice analog of the continuum result in Eq. (8). Thus, we can rotate the interaction Hamiltonian into the band basis according to $U^\dagger(\vec{k})H_{int}(\vec{k})U(\vec{k})$, which gives

$$H^b_{int}(\vec{k})=-\frac{e}{c}\frac{A_\mu}{|t(k)|}\begin{pmatrix}-\mathrm{Re}\,(t^*\partial_{k_\mu}t) & i\,\mathrm{Im}\,(t^*\partial_{k_\mu}t)\\ -i\,\mathrm{Im}\,(t\partial_{k_\mu}t^*) & \mathrm{Re}\,(t^*\partial_{k_\mu}t)\end{pmatrix}. \tag{37}$$

Explicit evaluation of the matrix elements in Eq. (36) for a general chiral nanotube is complicated. *In general*, one may have interband matrix elements between lowest subbands of a conducting tube [which are the off-diagonal terms in Eq. (37)]; albeit with greatly reduced magnitudes—the scale of these matrix elements is typically $\approx 10^{-2}$ the scale for the matrix elements in Eq. (31), which are produced by the mass term in the linearized theory for a semiconducting tube. An important exception to this rule for conducting tubes occurs for the armchair (M,M) tubes. Then one finds that $t(k)=e^{2\pi i/3}[1+2\cos(k_xa)]$ for propagation in the lowest subbands of the tube, and we have

$$[t^*(k_x)\partial_k t(k_x)]/|t(k_x)|=ta\,\mathrm{sgn}\,[1+2\cos(k_xa)]\sin(k_xa). \tag{38}$$

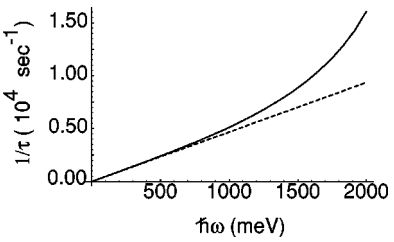

FIG. 5. Frequency dependence of the third-order transition rate involving the lowest subbands of a conducting zigzag tube, which produce an anisotropy of the photocurrent. The dashed curve uses a linear dispersion relation for the electronic states with the matrix elements computed using the lattice theory of Eq. (37). The normalization of the incident fields is the same as for the results of Fig. 4 so that the rates can be directly compared (note the vertical scale change). These interband excitations are symmetry forbidden in the Dirac theory but become weakly allowed in the presence of crystal-field effects on the low-energy electronic states. For a conducting tubes third-order transitions between the gapped subbands provide a much stronger nonlinear third-order response, as shown in Fig. 4.

Thus, near the critical points the diagonal elements of the velocity operator are $\pm v_F$ and the off-diagonal components vanish *everywhere*. Note that this occurs because of a tube symmetry; the armchair tube retains a mirror plane, which contains the tube axis so that the two lowest subbands of the conducting tube can be indexed as even or odd under reflection through this mirror plane. The vector potential along the tube axis is even under the mirror reflection and cannot couple even and odd subbands. On the other hand, for a zigzag tube one has $t(k)=e^{ik_y a/\sqrt{3}}(1+e^{-i\sqrt{3}k_y a/2})$. This vanishes for $k_y=2\pi/\sqrt{3}a$ which corresponds to a ''face'' of the Brillouin zone in Fig. 1. Thus, one finds for the conducting zigzag tube

$$(t^*\partial_k t)/|t| = \frac{ta\left[\frac{i}{\sqrt{3}}\cos^2(\sqrt{3}ka/4)\right]-\left[\frac{\sqrt{3}i}{2}\cos(\sqrt{3}ka/4)e^{\sqrt{3}ik_y a/4}\right]}{|\cos(\sqrt{3}ka/4)|}. \tag{39}$$

Therefore, near the crossing point $k_y=(2\pi/\sqrt{3}a)+q$ one finds

$$(t^*\partial_k t)/|t| \approx \frac{\sqrt{3}ta}{2}\left(1-i\frac{qa}{2\sqrt{3}}+\cdots\right). \tag{40}$$

Thus, the diagonal matrix elements of the velocity operator [the real part of Eq. (39)] are constant $[v_F(1+\mathcal{O}(qa))^2]$ while the off-diagonal elements (the imaginary part) vanish proportional to qa near the Fermi points. This implies that the product of the matrix elements in the third-order transition rate vanish as $(qa)^2$ for the conducting zigzag tube. This changes both the magnitude and the frequency dependence of the third-order transition rate. We obtain

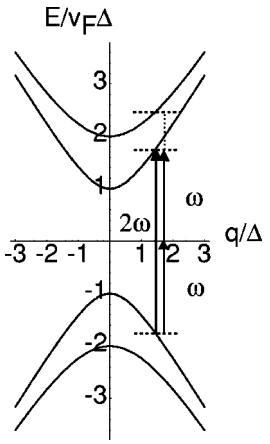

FIG. 6. Interfering excitations when the ω field is polarized perpendicular to the tube and the 2ω field is polarized along the tube direction. The 2ω field excites transitions between subbands with the same azimuthal quantum numbers. The ω field excites transitions with $\delta m=\pm 1$.

$$(\dot{\rho}_3)_{22}=\frac{\pi e^3 v_F}{12\hbar^2 c^3}a^2\omega\,\mathrm{sgn}(q)\,\mathrm{Re}\,(A_{2\omega}A_{-\omega}A_{-\omega} \times e^{i(\phi_2-2\phi_1)})\,\delta[2(|t(q)|-\hbar\omega)]. \tag{41}$$

The result is plotted in Fig. 5 using the same normalization as in Fig. 4 for comparison (note the scale change). One finds that the transition rate vanishes linearly in frequency, and is suppressed by $\approx 10^{-2}$ with respect to the interband transition rate for a semiconducting tube. This reflects the fact that at low-energy the effects of trigonal warping are relatively small compared to the backscattering from the mass term in the low-energy Hamiltonian for a semiconducting tube. We note that calculations of the frequency dependence of the resonant Raman cross section for conducting tubes[11] show a strong enhancement of the cross section near the first interband threshold, also demonstrating the suppression of interband transition matrix elements between the lowest conducting subbands in these structures.

Figure 5 presents *only* the results for excitations coupling the lowest subbands of a conducting tube. Transition rates between gapped subbands are described by Eq. (34) so that the transition rate displayed in Fig. 4 should be superposed on these results. This situation calculated for a zigzag tube illustrates the generic behavior for a general (M,N) tube if one wishes to calculate beyond the linearized theory. Analogous results for arbitrary chiral tubes can be obtained by direct evaluation of the matrix elements in Eq. (37).

C. Noncollinear fields

This treatment can be extended to include the situation where the exciting fields are not collinear. Interestingly, this does not change the qualitative frequency dependence shown in Fig. 4, although the prefactor is altered for noncollinear fields.

We will consider only the case where the exciting fields are orthogonal, since any incident field can be resolved into its longitudinal (along the tube) and transverse (perpendicular to the tube) components. We observe that for a field perpendicular to the tube axis we have allowed interband tran-

sitions only when the azimuthal quantum number m changes by ± 1 since the vector potential A ''seen'' in the tangent plane of the tube is $\vec{A}\cdot\hat{\phi}=A\cos\phi$ where $\hat{\phi}$ is a unit vector that circulates counterclockwise around the tube waist. For the graphene sheet this is equivalent to introducing a spatially varying vector potential with wavevector $1/R$ where R is the tube radius. Thus, the third-order nonlinear process we are seeking is symmetry forbidden if $\vec{A}_{2\omega}$ has a transverse polarization (the lowest subbands have the same azimuthal quantum numbers.) However, it is possible to have the situation shown in Fig. 6, where $\vec{A}_{\omega}$ is perpendicular to the tube axis, and $\vec{A}_{2\omega}$ is polarized along the tube direction. Here the virtual intermediate state for the two-photon process is provided by a higher azimuthal subband.

This reduces the strength of the effect, but not the overall frequency dependence, which is controlled by dispersion of the lowest azimuthal subband that is accessed to second order in $\vec{A}_{\omega}$.

We modify the interaction Hamiltonian Eq. (33) for the situation where the exciting radiation is polarized perpendicular to the tube direction. In the ''site'' basis one finds that the interaction Hamiltonian for this polarization is

$$H^{s}_{\alpha,int}=\frac{ev_{F}A}{c}\begin{pmatrix}0 & -i\\ i & 0\end{pmatrix}, \tag{42}$$

where $A=A(y)=A_0\cos(y/R)$. The y dependence implies that this interaction couples subbands with a difference in azimuthal quantum numbers m such that $\delta m=\pm 1$ and we will explicitly consider only the two low-energy pairs of subbands as shown in Fig. 6, which we label 1 and 2. The Hamiltonian in Eq. (42) can now be rotated into the band basis using the unitary rotations of Eq. (32) in the combination $H^{b}_{\alpha,int}=U_2^{\dagger}(q)H^{s}_{\alpha,int}U_1(q)$, which gives

$$H^{b}_{\alpha,int}=\frac{ev_{F}A}{c}e^{i(\gamma_2-\gamma_1)/2}\begin{pmatrix}\sin[\alpha(\gamma_1+\gamma_2)/2] & i\cos[\alpha(\gamma_1+\gamma_2)/2]\\ -i\cos[\alpha(\gamma_1+\gamma_2)/2] & \sin[\alpha(\gamma_1+\gamma_2)/2]\end{pmatrix}. \tag{43}$$

Thus, the second-order coherence term [analogous to Eq. (22) for the graphene sheet] is

$$(\rho_2)_{12}=-\frac{ie^2v_F^2A_{\omega}^2}{\hbar^2c^2}\frac{\alpha^2\sin(\gamma_1+\gamma_2)e^{-i(\Delta-2\omega)t}}{[-E_2(q)-E_1(q)+\omega-i\delta][-2E_1(q)+2\omega-i\delta]}. \tag{44}$$

The coherence factor appearing in Eq. (44) can be re-expressed in terms of the Hamiltonian parameters

$$\sin(\gamma_1+\gamma_2)=\frac{q(\Delta_2-\Delta_1)}{E_2(q)E_1(q)}, \tag{45}$$

where $E_m(q)=\sqrt{q^2+m^2\Delta^2}$ and Δ is the lowest gap of the semiconducting tube. Note that the effect vanishes for $\Delta_1=\Delta_2$, i.e. between subbands of the same azimuthal symmetry. The second-order coherence factor leads to the symmetry breaking third-order transition rate

$$(\dot{\rho}_3)_{22}=\frac{4\pi\alpha^2e^3v_F^3}{\hbar^3c^3\omega^4}\frac{(\Delta_2-\Delta_1)\Delta_1qE_1}{E_2}\mathrm{Re}(A_{2\omega}A_{-\omega}A_{-\omega}\times e^{i\phi_2-2i\phi_1})\delta[2(E(q)-\hbar\omega)], \tag{46}$$

which has exactly the same frequency dependence as the result of Eq. (34).

VII. DISCUSSION

Third-order phase coherent control of photocurrents have been studied and demonstrated for semiconductors [e.g., GaAs (Refs. 2, 3, and 13)] and since the effects calculated for carbon nanotubes are strongest for semiconducting tubes, it is appropriate to compare these effects. We find that the predicted effects are significantly stronger in nanotubes than for conventional semiconductors. This occurs because of the larger carrier velocities and the longer carrier relaxation times that are expected for the nanotubes. For carbon nanotubes this is particularly interesting since this third-order nonlinearity provides a method for current injection without contacts. It has proven experimentally difficult to fabricate low-resistance electrical contacts with carbon nanotubes by conventional submicron lithographic methods.

For an incident intensity $S=10^2$ kW/cm^2 the electric field amplitude $E=8.5\times10^5$ V/m$\approx10^6$ V/m. At an optical frequency $\omega=10^{15}$ s^{-1} this corresponds to a vector potential amplitude $|A|\approx10^9$ T$-$m (which is the value used in obtaining the results in Figs. 4 and 5). Then we find that the typical carrier injection rate $dn/dt\approx10^6$ s^{-1} per unit cell. For hot photoexcited carriers the relaxation rate is presumed to be dominated by phonon emission, for which we estimate a carrier relaxation time $\tau\approx1$ ps so the steady state distribution gives $\bar{n}\approx10^{-6}$ carriers per tube unit cell (note that the unit cell contains typically 40–60 carbon atoms around the tube circumference). Summing over the electron and hole contributions to the photocurrent and over the two electronic branches (K and K') we obtain an induced current $I\approx$ 0.4 nA, or an effective current density $J\approx260$ μA/μm^2. This is $10-10^2$ larger than the induced density predicted for third order transitions between the valence and conduction bands in GaAs.[13] The enhancement is due mainly to the relatively large carrier velocity for the carbon nanotubes, and the larger estimated carrier relaxation times. For conducting tubes this enhancement is partially offset by the *small* interband matrix

elements between the lowest subbands of conducting tubes; for a conducting zigzag tube we estimate the photocurrent density $J \approx 5\ \mu A/\mu m^2$ under the same assumptions, a value which is comparable to that found for conventional semiconductors.[13] We note that even with these long carrier relaxation times, one should be able to achieve a steady state distribution during a 100-ns incident pulse. For conducting nanotubes one has the additional difficulty of resolving this signal over a background free carrier density $\overline{n_b} \approx 10^{-5}$ produced by ordinary one-photon excitation between the lowest subbands [first term in Eq. (20)]. Since this is a ''nonpolar'' contribution, i.e., it does not contribute to the photocurrent, the nonlinear contribution can be identified, in principle.

The angular distributions calculated for interband excitations in graphene sheets show a similar structure to the angular dependence calculated for the third-order rate for transitions from the heavy-hole band to the conduction band in GaAs.[13] In both cases the net induced current is polarized along the direction of the exciting field, but the current distribution is peaked *away* from the field direction. The high symmetry of the graphene sheet provides an additional interesting degree of freedom, namely control of the direction of the injected current by controlling the *relative* polarizations of the incident fields, as displayed in Fig. 2. It would be very interesting to carry out experiments on graphite (either bulk or thin films) to verify the predicted angular dependence. Quantitative studies of the magnitude of the effect would be very useful as a probe of the scattering processes which control the dynamics of hot photoexcited carriers in these systems. We note that previous experiments on GaAs have observed the third-order nonlinearity, but with an amplitude that is an order of magnitude smaller than predicted theoretically.

For carbon nanotubes, one can anticipate at least three interesting applications of this phenomenon. First, as noted above, the method provides a means for current injection without electrical contacts. The absence of ''low resistance'' contacts on carbon nanotubes has often made it difficult to explore low-energy transport phenomena in these systems.[14–16] A particularly interesting experiment would be to use the third-order nonlinearity to produce a steady state separation of charge in a carbon nanotube rope or mat. In this state the ''driving force,'' which produces a photocurrent via the third-order nonlinearity would be balanced by the internal electric field produced by charge separation (in an open circuit condition). The relaxation of this charge distribution after the driving fields are turned off directly measures the conductivity *along* the pathways for charge motion in the system. Thus measurement of the transient relaxation after pulsed excitation would provide an interesting probe of the microscopic conductivity in this structurally heterogeneous system. Second, one can imagine applications that make use of the enhancement of the effect on semiconducting tubes (and its suppression in conducting tubes) to isolate semiconducting and conducting species in compositionally mixed samples. Finally, momentum transfer from the photoexcited carriers to intercalated ionic species can be used in principle to bias the diffusion of atomic or molecular species in the current carrying state. This effect requires *in addition* an asymmetry between the amplitudes for backscattering electrons and holes from the dopant species. This interesting application has been discussed in Ref. 5 using a simple model for the momentum transfer.

ACKNOWLEDGMENTS

We thank C. L. Kane for helpful comments about this problem. Work at Penn was supported by the DOE under Grant No. DE-FG02-84ER45118 and by the NSF under Grant No. DMR 98-02560. Work at Toronto was supported by Photonics Research, Ontario.

[1] G. Kurizki, M. Shapiro, and P. Brumer, Phys. Rev. B **39**, 3435 (1989).
[2] R. Anatosov, A. Haché, J. L. P. Hughes, H. M. van Driel, and J. E. Sipe, Phys. Rev. Lett. **76**, 1703 (1996).
[3] Y-Y. Yin, C. Chen, D. S. Elliot, and A. V. Smith, Phys. Rev. Lett. **69**, 2353 (1992).
[4] E. Dupont, P. B. Corkum, H. C. Liu, M. Buchanan, and Z. R. Wasilewski, Phys. Rev. Lett. **74**, 3596 (1995).
[5] P. Král and D. Tománek, Phys. Rev. Lett. **82**, 5373 (1999).
[6] C. L. Kane and E. J. Mele, Phys. Rev. Lett. **78**, 1932 (1997).
[7] M. O. Scully and M. Suhail Zubairy, *Quantum Optics* (Cambridge University Press, Cambridge, 1997), Chap. 5.
[8] J. W. Mintmire, B. I. Dunlap, and C. T. White, Phys. Rev. Lett. **68**, 631 (1992).
[9] N. Hamada, S. Sawada, and A. Oshiyama, Phys. Rev. Lett. **68**, 1579 (1992).
[10] R. Saito, M. Fujita, G. Dresselhaus, and M. S. Dresselhaus, Appl. Phys. Lett. **60**, 2704 (1992).
[11] E. Richter and K. R. Subbaswamy, Phys. Rev. Lett. **79**, 2737 (1997).
[12] P. L. McEuen, M. Bockrath, D. H. Cobden, Y. G. Yoon, and S. G. Louie, cond-mat/9906055 (unpublished).
[13] P. Král and J.E. Sipe, Phys. Rev. B (in press).
[14] A. Bezryadin, A. R. M. Verschuren, S. J. Tans, and C. Dekker, Phys. Rev. Lett. **80**, 4036 (1998).
[15] Ph. Avouris and R. Martel, *Physics and Chemistry of Nanostructured Materials* (Taylor & Francis, London, 1999).
[16] A. Bachtold *et al.*, Nature (London) **397**, 673 (1999).